Surface & Coatings Technology 481 (2024) 130675

Contents lists available at ScienceDirect

Surface & Coatings Technology

journal homepage: www.elsevier.com/locate/surfcoat

Influence of sputtering atmosphere on the structural, biological, and electrochemical properties of tantalum-containing coatings on the NiTi alloy

Mahdiyeh Soltanalipour [a], Jafar Khalil-Allafi [a,*], Amir Motallebzadeh [b]

[a] Research Center for Advanced Materials, Faculty of Materials Engineering, Sahand University of Technology, Tabriz, Iran
[b] Koç University Surface Science and Technology Center (KUYTAM), Koç University, Sariyer, 34450 Istanbul, Turkey

ARTICLE INFO

Keywords:
NiTi shape memory alloy
Tantalum coating
Tantalum oxide/nitride coatings
Magnetron sputtering
Sputtering atmosphere
Biological behavior

ABSTRACT

The magnetron sputtering method was used to deposit tantalum-containing coatings on NiTi shape memory alloys under Ar, Ar—O_2, and Ar—N_2 atmospheres. The main focus of this research is on how the deposition atmosphere can significantly impact not only the morphological and microstructural properties of coatings but also their corrosion behavior and in vitro biocompatibility. In this research, FESEM observations, GI-XRD crystallinity measurements, AFM topographical investigations, electrochemical measurements, and MTT assay were employed to determine to what extent the deposition atmosphere affects the morphology, microstructure, roughness, corrosion behavior, and in vitro biocompatibility properties, respectively. FESEM studies reveal that tantalum sputtered under the Ar atmosphere has a more uniform, and compact structure, while round-like particles appear on the surface under Ar—O_2 and Ar—N_2 atmospheres. The GI-XRD patterns indicate that the substrate temperature of 300°C is not sufficient for the formation of crystallized structure. It has been shown that the sample deposited under the Ar—N_2 atmosphere has more negative charges; this is associated with higher protein adsorption on its surface and increases endothelial proliferation rates. Moreover, the presence of Ta_2O_5 on the surface of the Ar—O_2 atmosphere leads to the highest corrosion resistance.

1. Introduction

Shape memory alloys (SMAs) have captured a great deal of interest in the scientific community, among which NiTi (Nitinol) alloys stand out as the top candidate, primarily because of their excellent mechanical properties, low elastic anisotropy, high superelasticity, biocompatibility, and corrosion resistance [1–3]. One of the notable features of this alloy is its unique strain recovery, which mimics the properties of human tissues and bones [4]. The reversible phase transformations of NiTi, known as the shape memory effect and superelasticity, take place since it can go through thermo-elastic phase changes as temperature and load vary [5]. Possessing a wide variety of characteristics, NiTi alloys are increasingly used in engineering and medical applications for manufacturing vascular stents and embolic filters [6].

Because of its stress-hysteresis and path dependence, NiTi alloy has biased stiffness, which is one of its most essential and rarely considered advantages. This feature is perhaps best used in stents [7]. However, a key factor for the surgery is the visibility of the stent under X-ray angiography. Unfortunately, NiTi alloys are radiolucent, meaning they let radiation pass through them because they have a low atomic number along with a low density. As a result, it would be naturally difficult to trace NiTi biomaterials in small dimensions, such as a brain stent with X-rays, once it has been placed in the patient's body [8,9]. Rapid dissolution of Ni ions in NiTi alloy crystal structure is also known to be allergenic and toxic to the human body [10,11]. Among various approaches to tackle this issue, it has been recommended to cover the outer area of the alloy with dense radiopaque materials [12]. The stents can usually become radiopaque by incorporating a radiopaque material with a high X-ray absorption coefficient [13]. Even a thin layer of a radiopaque material such as Ta, Au, Pt, or Ir makes the stent visible more efficiently under X-rays [14]. However, such elements are highly susceptible to galvanic corrosion of NiTi alloy owing to the considerable difference in corrosion potential between them [15]. Since Ta and NiTi have similar corrosion potential values, galvanic corrosion is

* Corresponding author at: Research Center for Advanced Materials, Faculty of Materials Engineering, Sahand University of Technology, P. O. Box: 51335-1996, Tabriz, Iran.
E-mail addresses: M_soltanalipour@sut.ac.ir (M. Soltanalipour), allafi@sut.ac.ir (J. Khalil-Allafi), amotallebzadeh@ku.edu.tr (A. Motallebzadeh).

https://doi.org/10.1016/j.surfcoat.2024.130675
Received 6 January 2024; Received in revised form 14 March 2024; Accepted 15 March 2024
Available online 18 March 2024
0257-8972/© 2024 Elsevier B.V. All rights reserved.

significantly retarded in Ta-coated NiTi alloy systems [7,16]. Additionally, tantalum turns into a passivating layer, making it corrosion-resistant in the human body [17,18].

It has been widely acknowledged that tantalum offers excellent magnetic resonance imaging (MRI) compatibility, corrosion-abrasion resistance, high radiopacity, hemocompatibility, and histocompatibility [10]. Moreover, it has been reported by many researchers that tantalum-based coatings like tantalum oxide, nitride, or oxynitride compounds substantially enhance endothelial cell activity compared with uncoated NiTi substrate [14,19,20]. Ta-based coatings can be deposited chemically, via techniques like electrodeposition, or physically by sputtering [11]. Magnetron sputtering (MS) is a particularly attractive technique for the deposition of tantalum-based coatings due to its ability to deposit materials with high melting points, relatively low deposition temperatures, ease of deposition on a variety of substrates with complex shapes, low surface roughness after deposition, excellent adhesion between coatings and substrate, cost-effectiveness, and ability to deposit highly pure and homogeneous nanometric multilayers over large areas [21–23].

This research investigates the possibility of forming a pure tantalum film and its several compounds, including oxide, nitride, and oxynitride, by sputtering the pure tantalum target in different atmospheres. Also, this paper examines how the deposition atmosphere influences the structure, morphology, roughness, corrosion behavior, and in vitro biocompatibility properties of tantalum-based coatings deposited on NiTi shape memory alloys by magnetron sputtering. Further, the influence of substrate temperature on the properties of Ta-based coatings is investigated in our previous research [24,25].

2. Materials and methods

2.1. Substrate preparation

As the substrate, 13 mm diameter and 2 mm thick disc-shaped samples were wire-cut from NiTi rods (with a nominal Ni content of 50.9 at. %). After grinding the samples with SiC emery paper 100–5000 grit, alumina slurry was used to finely polish the surfaces, followed by ultrasonic cleaning with acetone, ethanol, and distilled water, respectively. The samples were then dried at ambient air temperature.

2.2. Coating procedure

Using a dual-mode (DC and RF) reactive magnetron sputtering system (MECA-2000 model, France), the coatings were deposited on NiTi substrates. Pure metallic tantalum metal with 99.95 % purity was selected as a target for the deposition process. Because of the conductive character of the Ta target, a DC power source was used. It is worth mentioning that, this magnetron system has a thickness measuring device called THICKNESS MONITOR model TM_350 made by MAXTEK Inc. Initially, the magnetron chamber is evacuated to a pressure lower than 5×10^{-3} Pa. Before the deposition procedure, the target was pre-sputtered for 5 min using Ar (25 sccm, 200 W) as a sputtering gas, to remove any pollution from its surface. After entering the reactive gas and sputtering gas, the working pressure reached 5×10^{-1} Pa. Then, the substrate was sputtered using 25 sccm Ar gas with a DC power of 200 W. This procedure was done to create an interfacial layer up to 30 nm thickness. The interfacial layer improves adhesion between the substrate and the coating (second layer). The presence of this interlayer can decrease interface stress, increase coating adhesion and corrosion resistance, and reduce the mismatch in the performance of the ceramic coating and metal substrate, which is reported in the literature [26–28]. Then the second layer was deposited with a thickness of 400 nm. Throughout the deposition, to obtain a coating with uniform thickness and quality, the samples were rotated at a speed of 2 rpm (round per minute). A total thickness of nearly 400 nm was achieved by a thickness-measuring device.

The substrate temperature was set to 300 °C during the deposition process to increase adatom diffusion and eliminate the self-shadowing effect. As the temperature of the substrate increases, the energy of surface atoms also increases, causing them to vibrate and create cavities. The target atoms then penetrate these cavities, creating a denser and smoother structure. This phenomenon has been previously investigated in our research [24,25]. Generally, target poisoning occurs with a higher flow ratio of reactive gases (oxygen or nitrogen), >20 vol% of reactive gas. This means that the compound film is formed not only on the surface of the substrate but also on the surface of the target. As a result, the performance of sputtering is reduced and the deposition rate decreases [29]. Accordingly, to destroy the target poisoning effect (i) 100 vol% argon, (ii) 16.6 vol% oxygen, 83.4 vol% argon, and (iii) 16.6 vol% nitrogen, 83.4 vol% argon were selected as the gas composition of the sputtering atmosphere. Experimental data for the prepared coatings are presented in Table 1. It is worth mentioning that, to minimize internal stresses, coated samples were cooled to room temperature under a vacuum condition, before being exposed to air.

2.3. Characterization

To scrutinize the morphology and composition of coatings, the field emission scanning electron microscope (FESEM: MIRA3 FEG-SEM, Vega Tescan, Czech Republic) with an energy-dispersive X-ray spectrometer (EDS) functioned at 15 kV by Oxford Instruments were used. Before examining the samples using FESEM, a thin layer of Au had been applied to them.

The adhesion strength of the coatings was studied according to the ASTM F1044-05 standard. In this regard, the coated samples were glued to the NiTi substrate by 2214 Regular Epoxy Adhesive. To reach a bond strength of 50 MPa, it was placed at a temperature of 150 °C for 4 h. Finally, the adhesive pairs were pulled to the failure point using the Gotech-Al-7000 LA10 universal test machine at a 1 $mm.min^{-1}$ rate.

A Grazing Incidence X-ray Diffraction system (GI-XRD: PANalytical X'Pert Pro, Netherlands) equipped with Cu Kα as the radiation source was used to examine the crystalline phases of coatings. In this experiment, the applied voltage and current were 40 kV, and 30 mA, respectively. The X-ray incidence with an angle of 0.5° was used in this experiment. The scan speed was 0.02°/*sec*.

The chemical state of the constituent elements was characterized by Thermo Fisher Scientific K-Alpha X-ray photoelectron spectroscopy (XPS) with a source of monochromatic Al Kα (1486.6 eV). Before initiating the XPS test, the sputter cleaning process was carried out over a 400 × 400 μm^2 area of the films using a rastered 2 keV Ar^+ ion beam with the etching rate of 0.05 $nm.s^{-1}$ for 200 s to remove any surface contamination that may shatter the test results. Binding energies were determined by the peak at 284.6 eV of the C 1 s as the charge reference.

Atomic Force Microscopy (AFM; Model Nanosurf Mobile S, Switzerland) was used to analyze surface topography and roughness. It was equipped with a Tap 190 Al-G Probe, which was set to intermittent contact (tapping mode). The roughness parameters were averaged over eight measurements and reported for each.

Table 1
A description of deposition parameters for the tantalum-containing coatings on NiTi shape memory alloy by magnetron sputtering.

Sample code	Interlayer	Gas type and flow (sccm[a])	Substrate temperature (°C)
Ar-I-300	Yes	Ar = 25	300
O_2-I-300	Yes	O_2 = 5, Ar = 25	300
N_2-I-300	Yes	N_2 = 5, Ar = 25	300

[a] Standard cubic centimeters per minute.

2.4. Wettability measurements

Contact angle goniometers were used to measure coating wettability using the sessile drop method. Static contact angles were measured at room temperature in a static dispensing system (Jikan CAG-10, Iran). The examined samples were immersed in 70 wt% ethanol for 20 min to be fully sterilized before measuring the wetting angle. In this case, 2 μL of test liquid, deionized water, was injected at an average rate of 2 μL. s^{-1}. The measurement was repeated five times, and the average value was calculated and reported. Using commercial control, the bare NiTi substrate has also been tested with the water contact angle system to conclude the hydrophilicity of the surface. After 10 s, when the probe liquid droplet reached the equilibrium point, the angles were recorded.

2.5. Electrochemical measurements

The electrochemical behavior of the samples was investigated using the potentiodynamic polarization method (WonATech, Zive SP2, South Korea). The electrochemical cell contained a working electrode (coated/uncoated sample), a counter electrode (pure platinum electrode), and a reference electrode (Ag/AgCl-3M KCl). SBF solution was used as the test solution to simulate the corrosion environment with the ionic composition of human blood plasma ($T = 37\pm0.5$ °C). The solution was prepared according to the protocol suggested by Kokubo and Takadama [30]. It is noteworthy that all corrosion analyses were conducted in SBF solution at 37±0.5 °C to mimic the ionic composition of human blood plasma as much as possible. To obtain a stabilized open circuit potential, the samples were placed in the SBF solution for 2 h at a temperature of 37±0.5 °C, before each measurement. After reaching a constant potential, electrochemical impedance spectroscopy measurements (EIS) were performed at frequencies between 10 mHz and 100 kHz with a 10 mV AC voltage range. The ZView software was then used to determine the most suitable equivalent circuit to fit the obtained EIS spectra. Finally, the potentiodynamic polarization (PDP) was carried out with a scan rate of 1 $mV.s^{-1}$.

2.6. Biological behavior

2.6.1. MTT assay

First and foremost, the examined samples were immersed in 70 wt% ethanol for 20 min to be fully sterilized. The samples then were exposed to ultraviolet waves (UV Grade C-8 W) to be stored under sterile conditions. Human umbilical vein endothelial cells (HUV-EC-C C554) were cultured at a density of 10^5 cells per well. Cell viability was studied by the MTT method. To achieve this, the samples were placed on cell culture plates, and 1.5 mL of DMEM culture medium containing 10 % FBS was carefully added to the surface of each well after adding the cell suspension to each well. Samples were kept under those conditions for seven days.

MTT reagent was prepared (MTT concentration 5 mg/mL in PBS). Approximately 100 μL of MTT reagent was added to 900 μL of Dulbecco's modified eagle's medium (DMEM culture medium) to obtain a diluted MTT solution. To each sample in the culture container, 1 mL of diluted MTT solution was added and the samples were incubated at 37 °C for 2 h and covered with aluminum foil. Upon observing purple fermazone deposits under a microscope, a culture medium containing the MTT reagent was discarded, and 1 mL of acidic isopropanol (a solution containing 0.04 M HCl in absolute isopropanol) was added to each well to dissolve the fermazone crystals. The absorbance of fermazone crystals was measured at 570 nm wavelength with a UV reader. The experiment was repeated three times. MTT calculated the optical density of fermazone produced by living endothelial.

2.6.2. Apatite formation

The samples were soaked in 30 mL of SBF solution for 30 days at 37±0.5 °C and pH 7.4 to investigate their ability to form apatite. The solution was changed every 48 h to revive the solution concentration and pH level.

2.6.3. Nickel ion release

The samples were immersed in Ringer's solution for 30 days at 37±0.5 °C, with a volume of 10 mL. Following that, nickel ions released from the surfaces of the samples were determined by an inductively coupled plasma-optical emission spectrometry (ICP-OES; Varian model 730-ES, Germany). Using EPA7–1504-3001 standards, 1 mL of solution was analyzed.

3. Results and discussions

3.1. FESEM and EDS analysis

Fig. 1 illustrates the morphological FESEM images taken from the coated samples in different atmospheres. As shown below, in the left corner of Fig. 1(a, d, and g), in macroscopic images, the coated samples have a shiny and colored appearance. Fig. 1a, d, and g show a top view of the coatings with 100 vol% argon, 16.6 vol% oxygen, and 16.6 vol% nitrogen in the sputtering atmosphere. These FESEM images show relatively uniform coverage of the coatings, with no visible cracks.

The Ar-I-300 sample has a more uniform, and compact structure according to Fig. 1b, e, and h. Nevertheless, there are round-like particles that have appeared on the surface of samples O_2-I-300, and especially N_2-I-300. What is more, the high magnification images, Fig. 1c, f, and i, indicate that there are many nano-scaled voids among the columnar structures which aligns with the findings of the researchers [31,32]. Based on Fig. 1c, f, and i, it appears that nano-scaled voids in the O_2-I-300 sample are deeper than the N_2-I-300 sample. Additionally, the Ar-I-300 sample has a more compact structure compared to others. According to Donovan and Heinemann [33], the void network found in the amorphous film was formed due to the density-free boundaries inherent in it. As a result, the presence of nanoscale voids in the amorphous film could be the reason behind the void network structure observed in Fig. 1(c, f, i). Moreover, Fig. 2 shows a columnar structure in cross-sectional images of the deposited coatings. The thickness of the deposited coatings is close to the taken value. As can be seen, the thickness of sample O_2-I-300 is relatively high. It seems that the reason is the greater tendency of tantalum to react with oxygen. ASTM F1044–05 standard was used to measure the bond strength of the coating. The bond strength of the Ar-I-300, O_2-I-300, and N_2-I-300 are 47.8, 44.2, and 45.6 MPa, respectively. It appears that Ta-based thin films adhere well to the substrate surface since no tantalum flakes were observed on the bare substrate surface.

To obtain information about the elemental composition of the coatings, the EDS analysis was conducted. The results of the analysis are presented in Fig. 3, which provides valuable data regarding the specific elements present in the coatings. Intended for the same surface properties to be demonstrated, elements must be distributed uniformly throughout the coating. The elemental mapping indicated that Ta, O, and N atoms were evenly distributed within coating matrices.

As can be seen, the introduction of reactive gases (oxygen or nitrogen), led to a weaker observation of Ni and Ti elements, probably due to the presence of round-like particles in the coating. The atomic percentage of tantalum can serve as a reliable indicator of coating density. A denser coating is likely to contain a higher concentration of Ta. The Ar-I-300 sample has the densest coating, containing 41.22 at.% of Ta, and 4.23 at.% of O. Since, it is possible to incorporate oxygen at a pressure of 5×10^{-3} Pa, amounts of oxygen remain in the deposition chamber and enter the coatings. In the right corner of these figures, the ratio of oxygen to tantalum is calculated. In this sample, the O/Ta ratio is 0.1. As expected, in the sample O_2-I-300, the ratio of O/Ta has increased dramatically up to 0.66 and contained 23.97 at. % O. In the N_2-I-300 sample, which was deposited in 16.6 vol% nitrogen, and 83.4 vol% argon atmosphere, the amount of O was 3.35 at.%. The ratio of O/Ta is

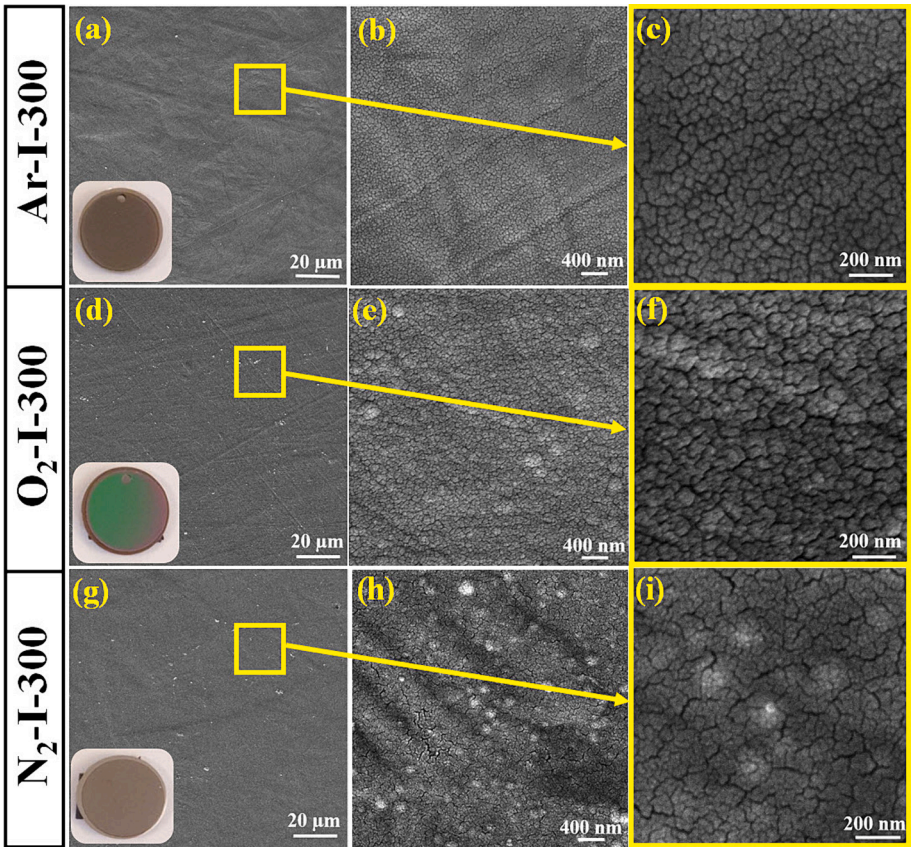


Fig. 1. Top view FESEM micrograph (a, d, and g), macroscopic images (the lower left corner of a, d, and g), morphology (b, e, and h), magnified view of the square box of the coatings deposited in different sputtering atmospheres (c, f, and i). The first, second, and third rows in the figure represent the tantalum-containing coatings deposited in (i) 100 vol% argon, (ii) 16.6 vol% oxygen, 83.4 vol% argon, and (iii) 16.6 vol% nitrogen, 83.4 vol% argon, respectively. FESEM micrographs are reserved in SE mode, which should be noted.

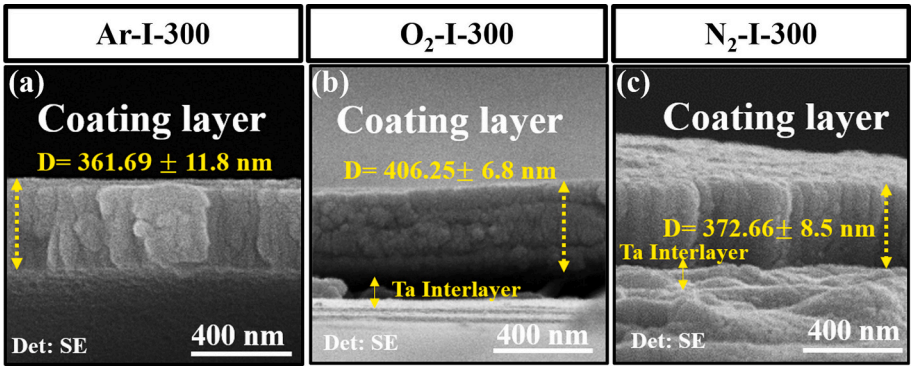


Fig. 2. FESEM Cross-sectional images of the deposited coatings in different sputtering environments: (a) 100 vol% argon, (b) 16.6 vol% oxygen, 83.4 vol% argon, and (c) 16.6 vol% nitrogen, 83.4 vol% argon.

0.09 for the N_2-I-300 sample. It can be inferred that the Ar-I-300 sample, deposited in the atmosphere containing 100 vol% argon, is composed of pure tantalum with minor amounts of oxide. Furthermore, the O_2-I-300 coating may comprise Ta_xO_y phases, while the N_2-I-300 coating may include some Ta_xN_y phases with partial oxidation.

3.2. GI-XRD analysis

The GI-XRD results of the tantalum-containing coatings are demonstrated In Fig. 4 at three dissimilar sputtering atmospheres. Amorphous structures are evident in each spectrum, as there are no visible sharp peaks in diffraction. The atoms in the coatings have low mobility because even 300 °C is very low compared to the melting point of tantalum (3017 °C), making it impossible for them to array themselves in a crystalline structure [34,35]. In their as-deposited state, all coatings are thus amorphous.

3.3. XPS analysis

In this experiment, an XPS spectrum is obtained, which is a plot of electron flux vs. binding energy. The XPS spectra of the as-deposited tantalum-containing coatings are shown in Fig. 5. As can be seen, these spectra include the major characteristic peaks of oxygen (O 1 s), tantalum (Ta 4f, Ta 4p, Ta 4d, and Ta 4 s), and a low-intensity peak of

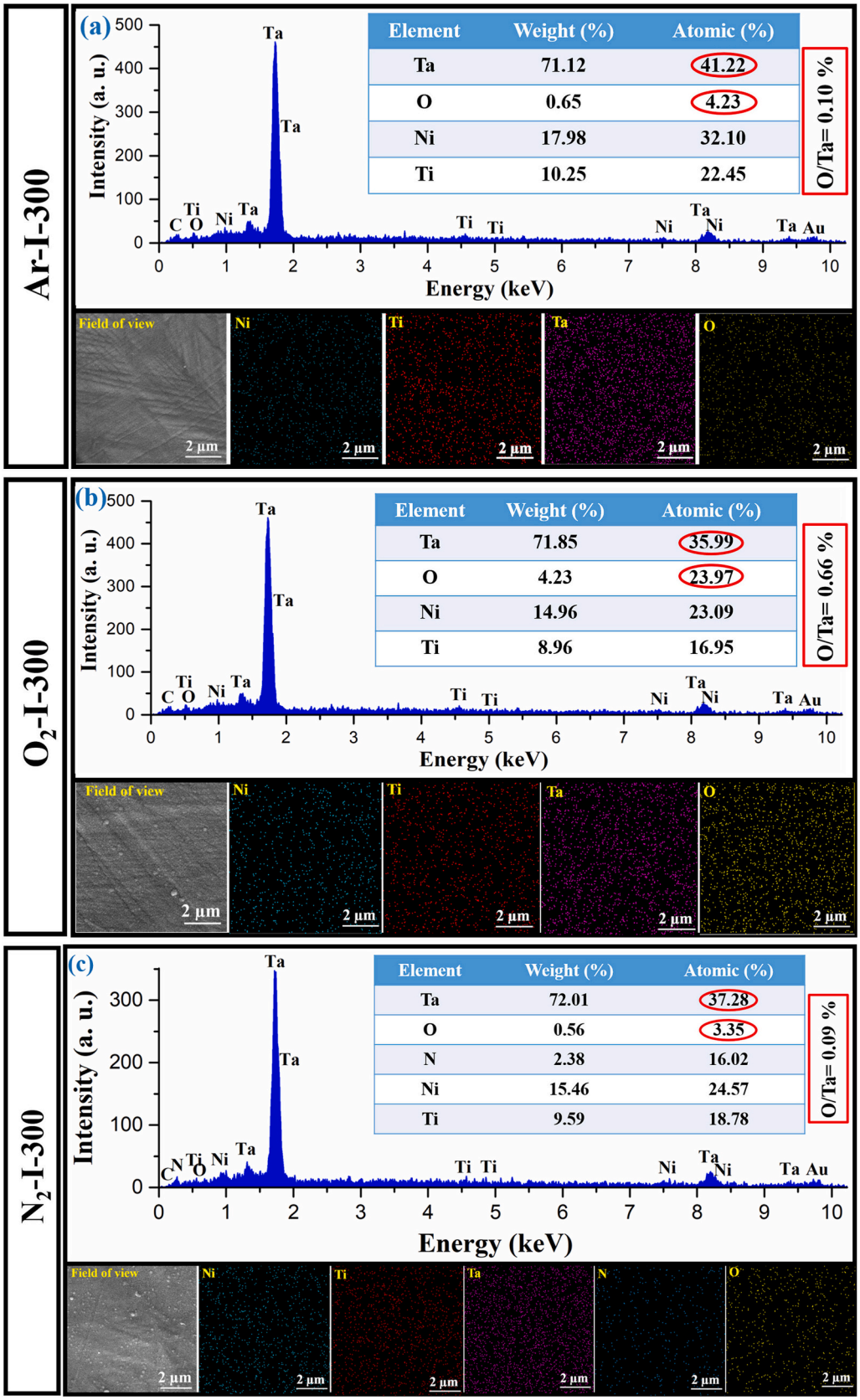


Fig. 3. The EDS analysis from the surface of coatings, along with the corresponding elemental map. Parts (a), (b), and (c) in the figure represent the tantalum-containing coatings deposited in (i) 100 vol% argon, (ii) 16.6 vol% oxygen, 83.4 vol% argon, and (iii) 16.6 vol% nitrogen, 83.4 vol% argon, respectively.

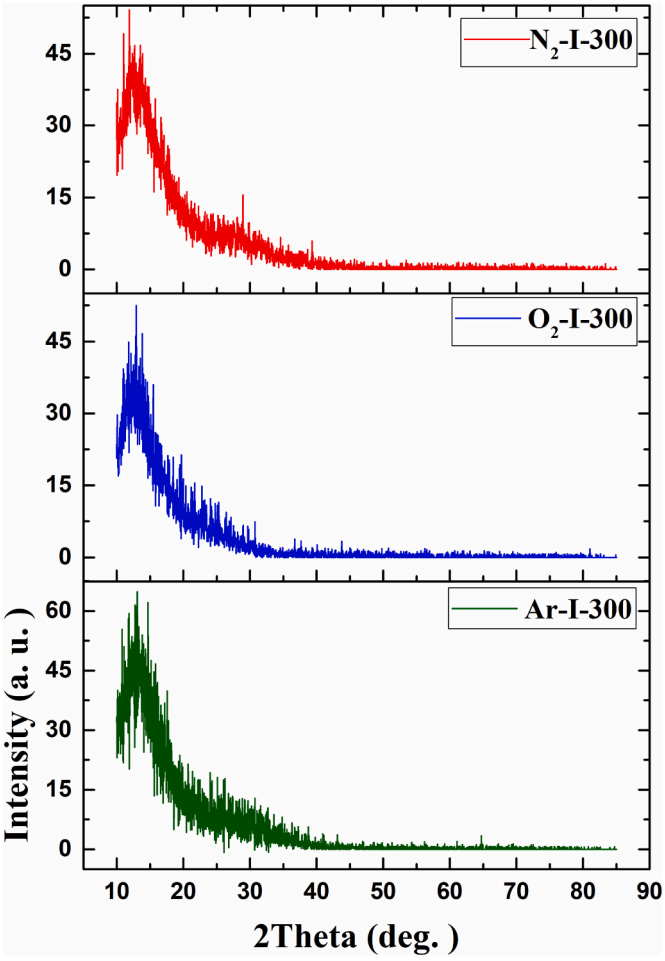


Fig. 4. The GI-XRD diffraction patterns of tantalum-containing coatings for a pure Ta metal target in the different sputtering atmospheres including (a) 100 vol% argon, (b) 16.6 vol% oxygen, 83.4 vol% argon, and (c) 16.6 vol% nitrogen, 83.4 vol% argon, respectively.

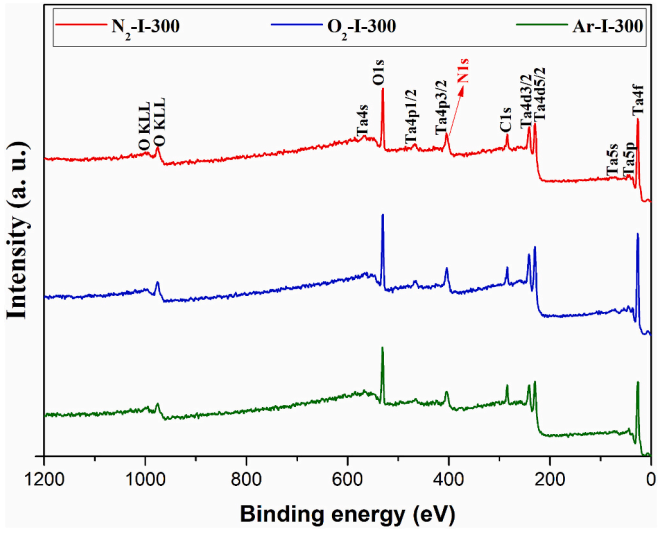


Fig. 5. XPS spectra of the as-deposited tantalum-containing coatings on NiTi substrate in a broad range.

carbon from contamination. Further investigation was carried out in a narrow spectrum as shown in Fig. 6. It is worthwhile to note that the process parameters, such as background pressure, target purity, and venting temperature, may influence the outcome of XPS analysis for films grown by PVD techniques. Low vacuum levels and/or low target purity levels are likely to result in the incorporation of carbon and oxygen into the layers, thereby making oxide-free core-level signals impossible. In the case of transition metals like tantalum, peak shapes often depend greatly on their chemical surroundings. For example, peaks for metallic samples tend to be asymmetric and become symmetric for their oxides [36]. As can be seen in Fig. 6, the Ta 4f peaks that appeared in the XPS results were symmetrical. It is possible to verify the structure states by examining the Ta 4f, O 1s, N 1s, and C 1s.

As can be seen in parts (a, d, and g) of Fig. 6, most of the species contain carbon-carbon bonds (peak C 1s at 284.6 eV) and carbon-oxygen bonds (peak C 1s at 288–288.9 eV), which are typical of surface organic contaminants of the outermost surface. As a result of the absence of carbon in coatings, there is no C 1s peak at 282.4 eV here [23].

As can be seen in parts (b, e, and h) of Fig. 6, the O 1 s spectrum shows an essential portion (red line) at 530.2 eV related to the oxygen-tantalum bond [37]. The O 1 s peak appearing at ≈ 529.7 eV (orange line) is also bonded to Ta, but the lower binding energy of this peak represents that this is a suboxide (TaO_x, $x < 2.5$) [11]. The peak (blue line, shifted by + 1.4 eV) and the second one (purple line, shifted by + 2.5 eV) can be devoted to adsorbed hydroxyl groups and carbonate species, respectively [38–40]. During sample transfer and storage, the surface oxidation and contamination of the coating resulted in the peak related to O—C binding [41].

Now the surface structure of the coated samples will be explained. As shown in Fig. 6(b, c), the binding energies of O 1 s and Ta $4f_{7/2}$ for the Ar-I-300 sample are 530.29 eV and 25.89 eV, respectively. This proves the presence of Ta_2O_5, the most stable oxidation state of tantalum. The Ta $4f_{7/2}$ line position at 20.87 eV, a shoulder at low energies proves the presence of the non-stoichiometric tantalum oxide (TaO_x $x < 2.5$) [10,42]. It may correspond to even lower oxidation states, that is mean Ta^+ [38,43]. These observations are also confirmed by the O 1 s spectrum (orange line in Fig. 6b). Based on the XPS results, the outmost surface of the Ar-I-300 sample is oxidized, containing a majority of Ta_2O_5 and a small amount of Ta_2O. In addition to amorphous Ta_2O_5, other Ta suboxides would appear, which is expected because the thin film is not heat-treated.

The XPS spectra of the O_2-I-300 sample are shown in Fig. 6(d, e, and f). The result demonstrated that as a result of oxygen gas entering the magnetron chamber, the coating exists only in the form of Ta_2O_5 because there is enough oxygen in the chamber. The results do not reveal the presence of any other Ta oxides. The Ta 4f (Ta $4f_{7/2}$ at 25.88 eV and Ta $4f_{5/2}$ at 27.78 eV) matched the binding energies of core levels of the Ta^{5+} atom in fully oxidized stoichiometric Ta_2O_5. This is also confirmed by the O 1 s peak located at a binding energy of 530.15 eV (see Fig. 6e).

The XPS spectra of the N_2-I-300 sample are shown in Fig. 6(g–j). By nitrogen gas entering the magnetron chamber, the results demonstrate that the Ta 4f spectra have shifted to lower binding energy, which is shown in Fig. 6(j). N_2-I-300 has binding energies of O 1 s (530.18 eV), N 1 s (399.96 eV), and Ta 4f (Ta $4f_{7/2}$ at 25.79 eV and Ta $4f_{5/2}$ at 27.69 eV). In the high energy spectra of Ta $4p_{3/2}$ or N 1 s, two chemical states are observed, at 399.96, and 404.12 eV, respectively, as can be seen in Fig. 6 (h–j). These chemical states correspond to Ta—N, and Ta—Ta bonds, respectively [41,44]. The binding energy of Ta $4p_{3/2}$ and N 1 s are very close to each other, as can be seen in the whole spectra (Fig. 5). In Fig. 6 (i) we see the broad spectrum, which seems to be overlapping two spectra of N 1 s and Ta $4p_{3/2}$. Furthermore, it is well known that an oxide layer can be formed on the surface of tantalum-based alloys [45]. It is noteworthy that, the XPS can provide information from the top layer of the coating up to a depth of approximately 10 nm [42], therefore due to the presence of this passive layer, the intensity of the nitrogen peak can

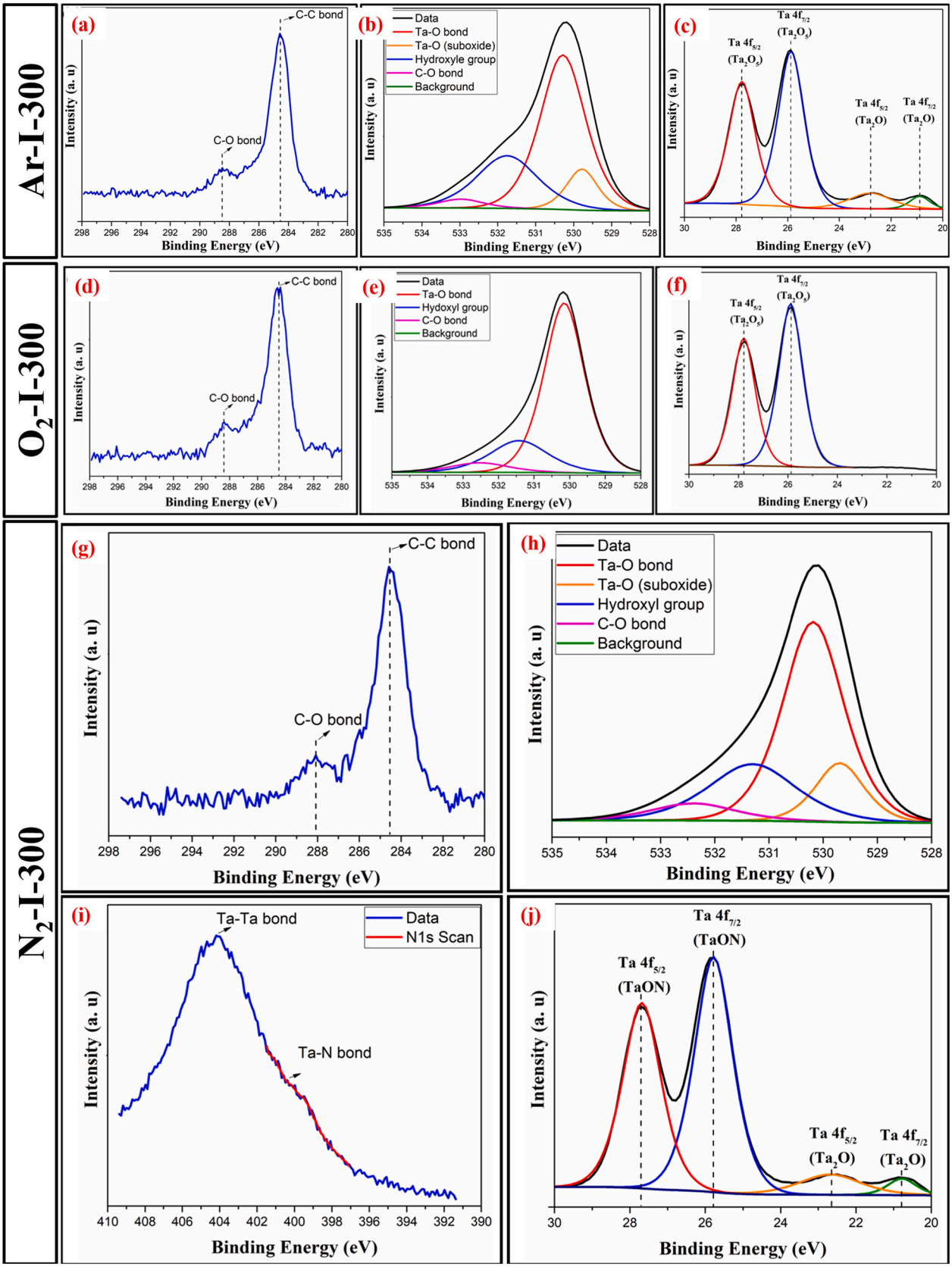


Fig. 6. High resolution of C 1s (parts a, d, g), O 1s (parts b, e, h), N 1s (part i), and Ta 4f (parts c, f, j) regions of the as-deposited coatings on NiTi substrate. The first, second, and third rows in the figure represent the tantalum-containing coatings deposited in (i) 100 vol% argon, (ii) 16.6 vol% oxygen, 83.4 vol% argon, and (iii) 16.6 vol% nitrogen, 83.4 vol% argon, respectively.

be reduced.

The TaON layer has formed on the surface because the Ta 4f peaks shifted to lower energy compared to pure Ta_2O_5 coating [46,47]. As a result of the more excellent covalent bond between Ta and N than between Ta and O, where oxygen is more electronegative than nitrogen, the binding energies shift to lower energy [47]. As shown in the O 1 s, N 1 s, and Ta 4f spectrum in Fig. 6(h–j), Ta exists in this coating as TaON and a small fraction of TaO_x ($x < 2.5$), possibly representing the even lower oxidation state Ta^+ [38]. Since Ta is a transition metal with a high affinity for oxygen, the XPS results indicated different Ta oxidation states. The oxide layer film is formed on top of the coatings when oxygen is incorporated during the deposition process or sample transfer and storage [41].

3.4. AFM analysis

Fig. 7 shows three-dimensional (3D) atomic force microscope images of bare NiTi and coated samples. AFM topographical images are used to discuss further the impact of the sputtering atmosphere on the surface topography of deposited films, including arithmetic average roughness (R_a), root-mean-square roughness (RMS, R_q), maximum peak height above the mean line (R_p), maximum valley depth below the mean line (R_v), and total roughness ($R_t = |R_p| + |R_v|$). Table 2 illustrates the results. The bare NiTi is a mirror-polished surface that is presented. As shown in Fig. 7d, N_2-I-300 tends to have the roughest surface ($R_q = 6.54 \pm 0.66$ nm). This tendency to be rough may be caused by reduced atom mobility due to the formation of Ta—N bonding during deposition, which aligns with the findings of the researchers [47]. Accordingly, among the coated samples, O_2-I-300 had the lowest roughness ($R_q = 2.26 \pm 0.63$ nm), indicating that the presence of oxygen promotes the densification of the coating, which is in agreement with the work of other researchers [48].

Table 2
The topographical parameters of tantalum-containing coatings based on AFM images.

Sample code	R_a (nm)	R_q (nm)	R_p (nm)	R_v (nm)	R_t (nm)
Bare NiTi	1.50 ± 0.09	1.85 ± 0.08	3.56 ± 0.75	−4.38 ± 0.90	7.94
Ar-I-300	2.60 ± 0.26	3.20 ± 0.29	8.25 ± 1.15	−7.93 ± 0.90	16.18
O_2-I-300	1.80 ± 0.43	2.26 ± 0.63	4.45 ± 0.94	−5.90 ± 2.36	10.35
N_2-I-300	5.25 ± 0.43	6.54 ± 0.66	14.02 ± 2.60	−14.59 ± 2.49	28.61

3.5. Contact angle

Surface wettability is a key factor that influences cell attachment and proliferation [49]. A biomaterial with a hydrophilic surface (contact angle <90°) is more likely to stimulate early cellular reactions, including cell adhesion, spreading, and proliferation, compared to a hydrophobic surface [18].

The wetting behavior and average contact angle of the samples are

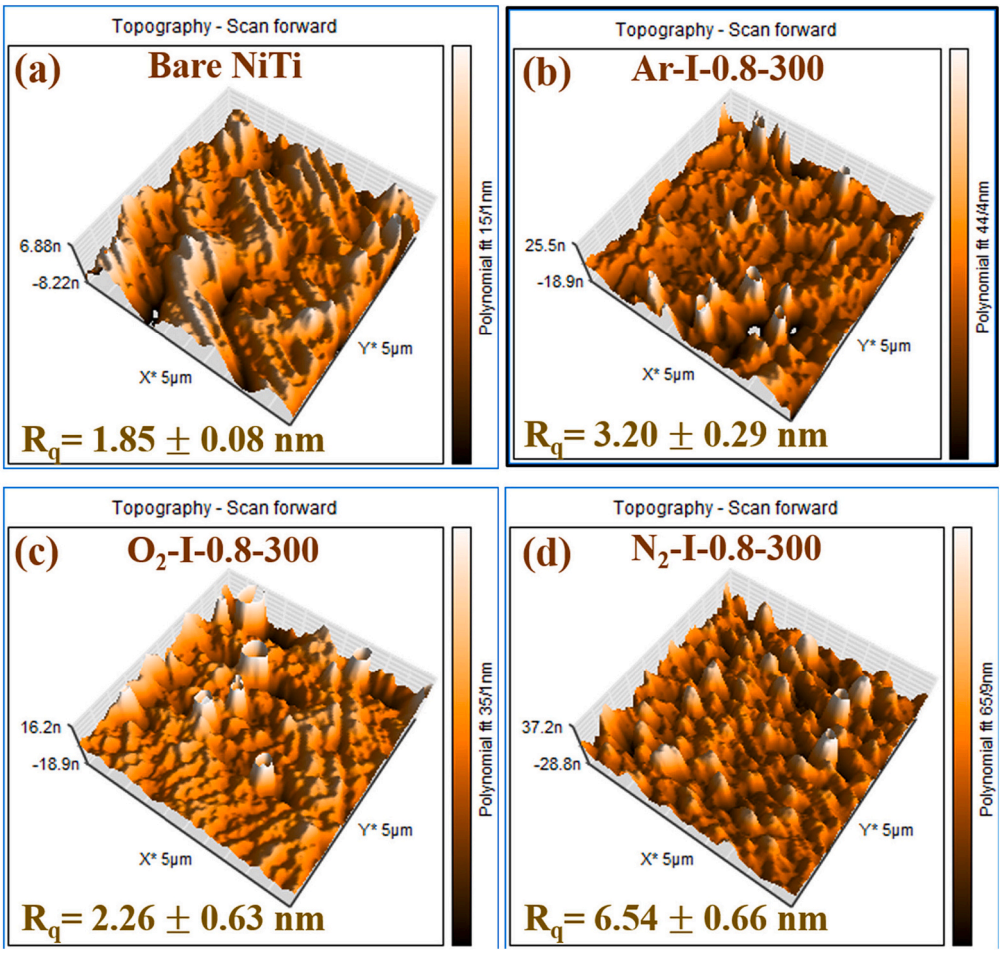


Fig. 7. Three-dimensional AFM topographical images of (a) bare NiTi substrate as well as tantalum-containing coatings deposited in the dissimilar sputtering atmosphere, containing: (b) 100 vol% argon, (c) 16.6 vol% oxygen, 83.4 vol% argon, and (d) 16.6 vol% nitrogen, 83.4 vol% argon, respectively are shown. AFM micrographs are acquired in tapping mode over a scanning area of 5 × 5 μm^2.

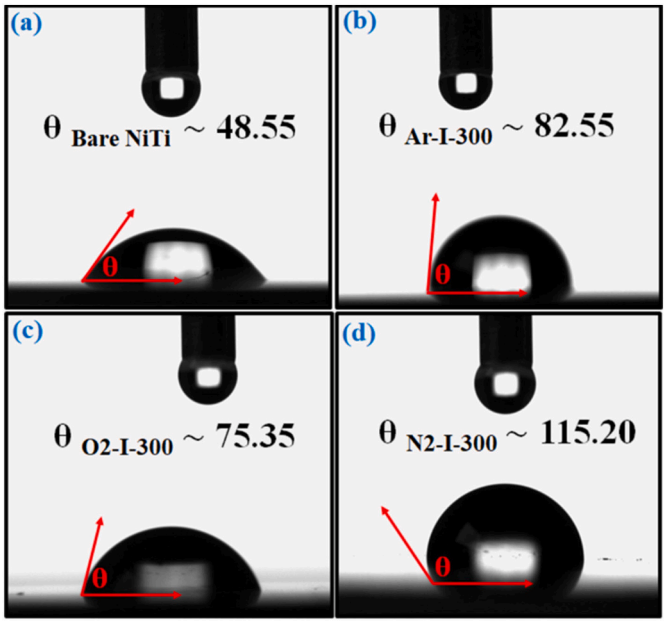


Fig. 8. Deionized water contact angles for (a) bare NiTi substrate as well as the tantalum-containing coatings deposited in (b) 100 vol% argon, (c) 16.6 vol% oxygen, 83.4 vol% argon, and (d) 16.6 vol% nitrogen, 83.4 vol% argon, respectively.

shown in Fig. 8. As can be seen, the coated samples had higher water contact angles compared to the uncoated ones. Figs. 7 and 8 show a strong relation/correlation between contact angle and surface roughness. In the Wenzel model, the water contact angle is inverse to the roughness [50]. However, in this research, the opposite results were obtained. In addition to the topography, the wettability of a surface depends largely on its surface chemistry [49]. Generally, Ta—O bonds tend to be hydrophilic while Ta—N bonds tend to be hydrophobic. Accordingly, among the coated samples, a greater level of hydrophilicity was observed for O_2-I-300 (75.35° ± 2.48). Conversely, the N_2-I-300 sample has the highest water contact angle (115.20° ± 2.42).

3.6. Electrochemical measurements

3.6.1. Potentiodynamic polarization

Biomaterials have long been used in aquatic environments where various types of anions, cations, organic matter, and dissolved oxygen are abundantly present. During local corrosion of NiTi biomaterial, Ni ions are released into the tissue surrounding it and enter the blood. Eventually, re-surgery is necessary due to infection, inflammation, and allergic reactions [51]. For this reason, its electrochemical behavior is necessary to be investigated. The results of the potentiodynamic polarization, depicted in Fig. 9, and the extracted data have been tabulated in Table 3. The Tafel extrapolation method was used to calculate corrosion potential (E_{corr}), cathodic region slope (β_c), anodic region slope (β_a), and corrosion current density (i_{corr}). Moreover, the corrosion protection efficiency (P.E), introduced in Table 3, was calculated using the following equation;

$$P.E(\%) = \frac{I^0_{corr} - I^c_{corr}}{I^0_{corr}} \times 100 \quad (1)$$

In the above equation, I^c_{corr} and I^0_{corr} are representatives of the corrosion current density in the presence and absence of the coating, respectively.

Corrosion potential designates the driving force required to initiate the corrosion of a material in a corrosive environment [52]. According to Fig. 9, and Table 3, the NiTi substrate had the highest corrosion potential (E_{corr}), thus it is the least prone one to corrosion from a thermodynamic point. On the other hand, corrosion current density (I_{corr}) is proportional to the flow of electrons on the surface exposed to corrosion, so the higher the corrosion current density, the higher the corrosion rate. After the deposition process, the corrosion current density decreased significantly compared to the substrate. In other words, the coating acted as a physical barrier and prevented corrosive ions from entering the metal surface. The O_2-I-300 sample showed the lowest corrosion current density value (1.22×10^{-6} mA.cm^{-2}) and the highest protection efficiency (99.74 %). Therefore, this sample released metal ions into the physiological environment at the slowest velocity. The smooth topography of this sample (R_q = 2.26±0.63 nm) could be a reason for this. It should be mentioned that the presence of the Ta_2O_5 phase on the outer surface of this sample is the main reason for the highest corrosion protection efficiency. The N_2-I-300 sample was characterized by the highest value of corrosion current density (1.09×10^{-4} mA.cm^{-2}), and the lowest protection efficiency (77.29 %). Its surface roughness (R_q = 6.54±0.66 nm) could be a reason for inferior corrosion properties. It is well known that inhomogeneities and irregularities in the surface could lead to the formation of local anodes, thereby increasing the corrosion rate.

The presence of a passive layer plays an important role in the corrosion behavior. The passivation current density (and breakdown potential) rather than the corrosion current density (and polarization resistance) should be considered when the samples experience passivation. As shown in Fig. 9, the passive layer of TiO_2 on bare NiTi collapsed

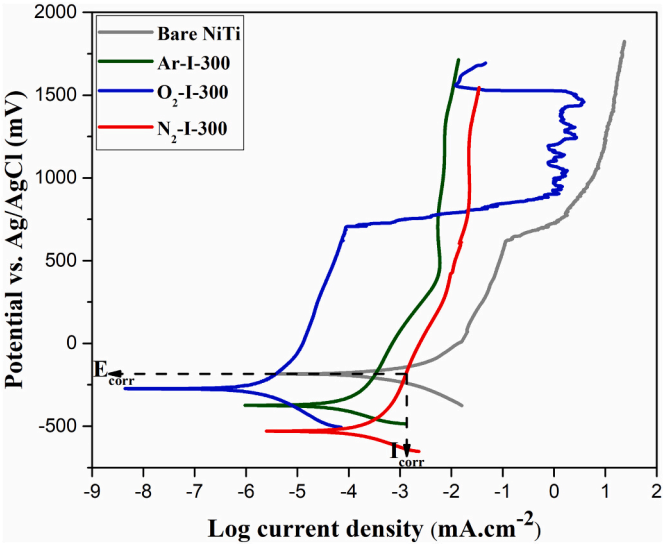


Fig. 9. Potentiodynamic polarization curves in SBF solution at 37 °C for bare NiTi substrate as well as the tantalum-containing coatings deposited in the different sputtering atmosphere.

Table 3
Electrochemical parameters extracted from potentiodynamic polarization curves for NiTi substrate and the tantalum-containing coatings.

Sample code	E_{corr} ($mV_{Ag/AgCl}$)	β_c (mV/decade)	β_a (mV/decade)	I_{corr} (mA.cm^{-2})	P.E[a] (%)
Bare NiTi	−183.72	83.13	96.24	4.80×10^{-4}	–
Ar-I-300	−373.84	92.63	175.85	4.53×10^{-5}	90.56
O_2-I-300	−271.91	119.32	178.65	1.22×10^{-6}	99.74
N_2-I-300	−529.78	102.74	172.53	1.09×10^{-4}	77.29

[a] Corrosion Protection Efficiency (P. E) was calculated from Eq. (1).

at a potential of about 606 mV vs. Ag/AgCl. This passive layer formed again at a current density of 14.79 mA.cm^{-2} on the surface. The coated samples quickly underwent passivation without the active-passive region. This linear and rapid transition from active to passive state indicates that all coatings undergo spontaneous passivation in solution and exhibit high chemical stability, which aligns with the findings of the researchers [53]. The passive layer on the O_2-I-300 sample broke at a potential of about 702.89 mV vs. Ag/AgCl, consequently the current increased rapidly. The formation of a new passive layer on the intermediate Ta layer was completed at the potential around 1534 mV vs. Ag/AgCl, and the current reached the minimum value of 0.012 mA.cm^{-2}. In contrast, the passive layer on the surface of N_2-I-300 and Ar-I-300 was relatively stable. The findings of researchers suggest that the hydrophobicity of a surface plays a crucial role in the formation of a stable passive layer on the surface [54]. The passive current density for the Ar-I-300 and the N_2-I-300 sample is 8×10^{-3} and 2×10^{-2} mA.cm^{-2}, respectively. The faster the passive layer forms, the lower the passive current density goes. Furthermore, the higher the break potential, the denser and more stable the formed passive layer. As a result, the passive layer forms at a relatively faster rate on the surface of the Ar-I-300 sample than on the N_2-I-300 sample. The topography of the surface and its compactness affect passive behavior.

Having a better understanding of the corrosion mechanism of tantalum-containing coatings in physiological environments will help reduce the degradation of metals in the body. The deposition of these coatings on NiTi alloy results in increased breakdown potential and passive areas for the Ar-I-300, and N_2-I-300, especially. As a result of the following reactions, a nanometer-thick passive layer protects the alloy from the damaging effects of the corrosion environment [40,55].

Anodic reaction

$$Ta = Ta^{5+} + 5e^{-} \tag{2}$$

Cathodic reaction in neutral or basic solution

$$O_2 + 2H_2O + 4e^{-} = 4(OH)^{-} \tag{3}$$

Overall reaction

$$4Ta + 5O_2 + 10H_2O = 4Ta(OH)_5 \tag{4}$$

Metal corrosion occurs as a result of electron exchange between the corrosive liquid and the metal surface, explaining the mechanism behind material corrosion [56]. During the process, metal atoms lose electrons

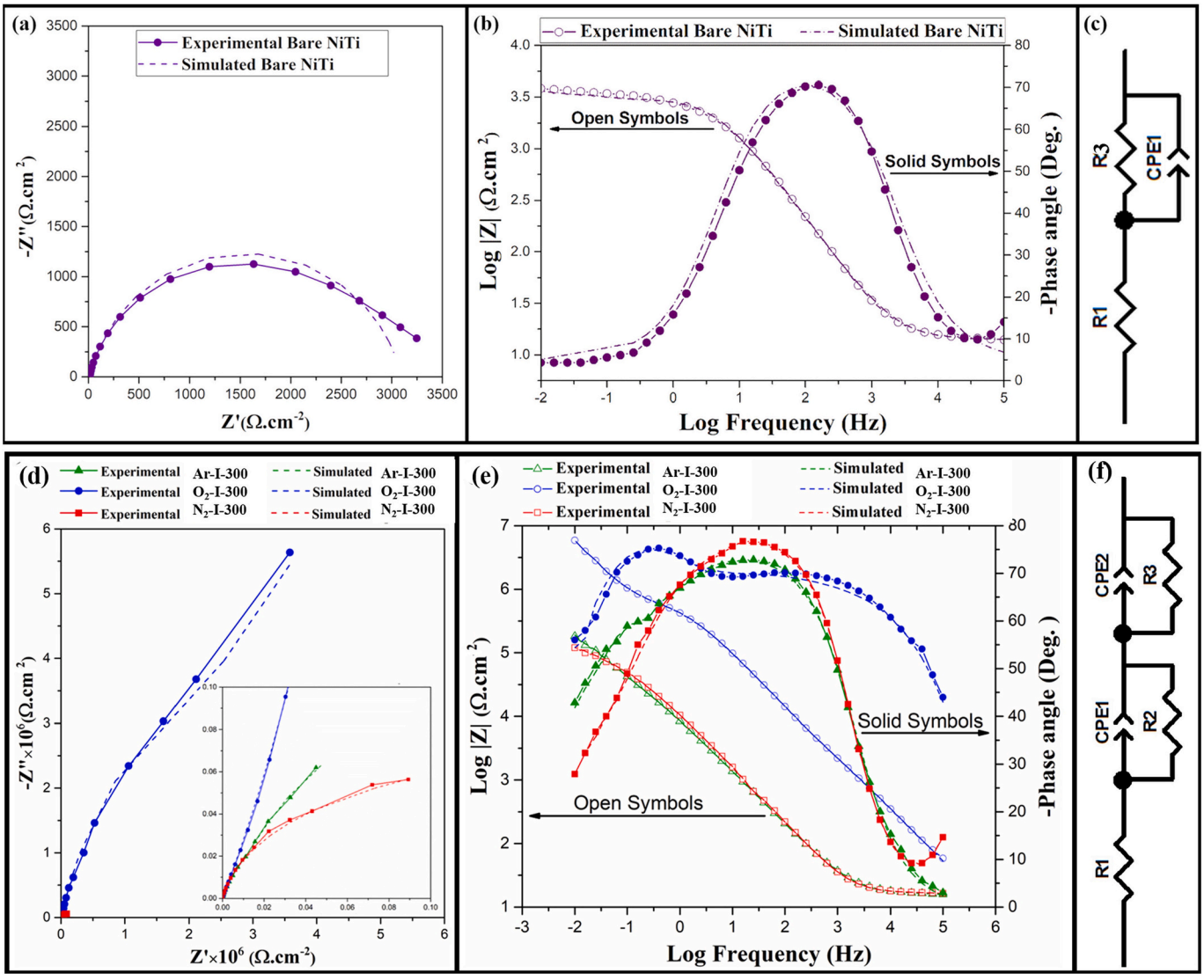


Fig. 10. Nyquist and Bode-Phase plots, and equivalent circuit models for bare NiTi substrate (parts a, b, and c), and tantalum-containing coatings deposited in the dissimilar sputtering atmosphere (parts d, e, and f). In the lower right corner of part d, the high-frequency region of Nyquist is inserted.

at the anode, generating positively charged ions, while oxygen and water molecules react at the cathode, forming hydroxide ions. These ions then combine to form metal hydroxide.

Its excellent mechanical properties and corrosion resistance make tantalum an ideal biological material for the human body and other living organisms. Tantalum is commonly observed without corrosion products whether in a lab environment or inside a living organism [57].

3.6.2. Electrochemical impedance spectroscopy

Electrochemical impedance spectroscopy investigations of coated and uncoated samples were performed in their respective E_{ocp} values to gain a deeper understanding of the corrosion behavior. The impedance spectrum of the uncoated one, and coated samples in the form of Nyquist (a, d), Bode-Phase plots diagrams (b, e), and equivalent circuit (c, f) are illustrated in Fig. 10. As can be seen (Solid symbols in parts b, and e), the maximum angle in the curves is <90 and shows that the surfaces have acted like a non-ideal capacitor. Therefore, instead of the capacitor in the equivalent circuit, a CPE is placed [58].

The NiTi substrate was modeled by a simple Randles equivalent as shown in Fig. 10c. Researchers have found that bare NiTi substrate has a relatively stable TiO_2 passive layer on the surface, which limits local corrosion. This is indicated in the Bode-Phase diagram where there are no peaks at high frequencies [59]. Two CPE must be present in the equivalent circuit of the coated samples because two peaks are observed in the Phase diagrams for all the coated samples. Also, in Nyquist diagrams, two semicircles are observed. The R_1 (Q_1R_2) (Q_2R_3) model has been used to model coated samples. This particular circuit is suitable only in cases where the coatings are free of cracks, and their conductivity is negligible [24]. The SBF solution contains many ions leading to numerous reactions and sediment formation. The first peak in the phase diagram is due to new sediments formed on the surface from various reactions in SBF. The second peak indicates the electrochemical charge transfer reaction at the electrode/electrolyte interface [52]. Table 4 provides a summary of the impedance parameters based on the proposed equivalent circuit models, as below;

R_1: The electrolyte resistance,
R_2: Resistance of the outer sediments layer,
CPE_1: The constant phase elements display the outer sediments layer,
R_3: Charge transfer resistance within the electric double-layer at the electrode/
electrolyte interface,
CPE_2: The constant phase elements demonstrate a double-layer capacitor formed at the electrode/electrolyte interface [49].

The larger the R_2 value, the denser the coating is, which means that there are almost no open pores available for the electrolyte to enter. Similarly, a larger R_3 value indicates the presence of a thin sediment layer between the electrolyte and the coating, which slows down the electrochemical dissolution process [58]. The constant CPE_1 at high frequency is linked to the dielectric properties of a coating, as well as its resistance to electrolyte attack in nanopores. Meanwhile, the constant CPE_2 at low frequency is associated with the electrochemical reaction of a double-layer capacitor made at the electrode/electrolyte interface [60].

The Nyquist diagram provides clear evidence that the diameter of the semicircles is directly related to the corrosion resistance of the surface. A larger diameter undeniably indicates the presence of a higher corrosion resistance. It is worth noting that the effectiveness of corrosion resistance can also be determined by examining the Bode plots. The plots that are positioned above others can indicate better corrosion resistance. Among the coated samples, the O_2-I-300 sample had the largest diameter, and the smallest value corresponds to the N_2-I-300 sample. It can be concluded that the coatings formed under the Ar—O_2 condition exhibited greater resistance against the corrosive species present in the solution. Table 4 contains several data points, but R_3 is particularly significant as it directly describes the charge transfer resistance. As can be seen, the R_3 value for O_2-I-300 (1.15×10^7 Ω.cm^2) is the largest, while it is the least for N_2-I-300 (1.29×10^5 Ω.cm^2), based on previous arguments.

Note that the superior corrosion resistance of the coatings formed under Ar—O_2 condition is mainly due to the Ta_2O_5 phase. Furthermore, the smoothness of the topography contributes to corrosion resistance. Based on the information provided, it can be concluded that the coatings formed at a mixture of Ar and O_2 atmosphere have demonstrated more efficient resistance against the intrusion of corrosive ions. These results are in agreement with the above potentiodynamic polarization results.

3.7. A survey on biological behavior

3.7.1. Cytotoxicity assay

The MTT test enables the quantitative determination of cell viability. Cell viability percentage was calculated from the following equation [61]:

$$\text{Cell viability } (\%) = \frac{\text{Experimental value}}{\text{Negative control}} \times 100 \quad (5)$$

Cell viability results for coated and uncoated cells are shown in Fig. 11 after seven days of culture compared to the negative control sample (untreated cells). According to the UNE-EN ISO 10993-5 standard, the percentage of cell survival must exceed 80 % to ensure the non-toxicity of the samples.

Unlike the coated samples, the bare substrate showed toxic behavior after seven days of culture. The reason is the excessive accumulation of nickel ions in the culture medium. In general, rapid dissolution of nickel ions is considered to cause toxicity and slow cell proliferation [14]. Surface chemistry and charge are the main factors that affect the initial absorption of proteins and cell proliferation [62]. The Ar-I-300 sample, deposited in the atmosphere containing 100 vol% argon, is composed of pure tantalum with minor amounts of oxide as confirmed by EDS (see Fig. 3). Accordingly, the Ar-I-300 sample was biocompatible and showed no toxicity behavior based on the percentage of cell viability. Thus, it can serve as a biocompatible coating for NiTi alloy, which has the best potential for use in stents. Cell proliferation in O_2-I-300 and N_2-I-300 samples indicated that both coatings were bioactive. Among the coated samples, the O_2-I-300 sample had a higher degree of hydrophilicity (75.35°±2.48), so primary cell responses such as cell adhesion, expansion, and proliferation are more strongly stimulated. Moreover, surface roughness is an important factor for cell behavior. Since the surface of the N_2-I-300 sample exhibited the highest roughness parameter compared to the others, therefore the most cell proliferation occurred on its surface.

Table 4
The EIS fitting results, calculated using EEC for both bare NiTi substrate and coated samples in SBF solution at 37 ± 0.5 °C.

Sample code	R_1 (Ω·cm^2)	CPE-T_1 (F·cm^{-2})	n_1 –	R_2 (Ω·cm^2)	CPE-T2 (F·cm^{-2})	n_2 –	R_3 (Ω·cm^2)
Bare NiTi	14.07	–	–	–	1.85×10^{-5}	0.86	3.08×10^3
Ar-I-300	15.88	4.76×10^{-5}	0.79	1.42×10^4	4.33×10^{-5}	0.89	2.02×10^5
O_2-I-300	34.26	7.45×10^{-6}	0.66	2.51×10^5	1.43×10^{-6}	0.88	1.15×10^7
N_2-I-300	16.43	2.57×10^{-5}	0.85	4.15×10^4	7.04×10^{-5}	0.86	1.29×10^5

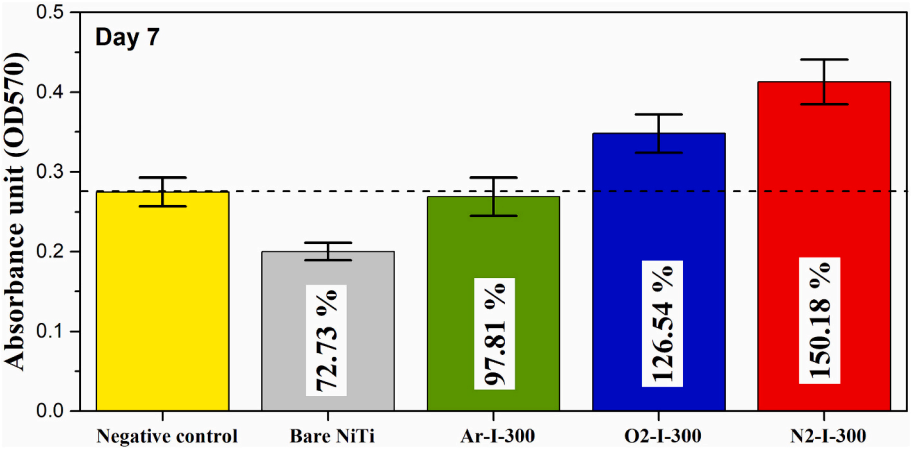


Fig. 11. Evaluation of endothelial cell proliferation cultured on bare NiTi substrate, and tantalum-containing coatings deposited in the dissimilar sputtering atmosphere using the MTT method.

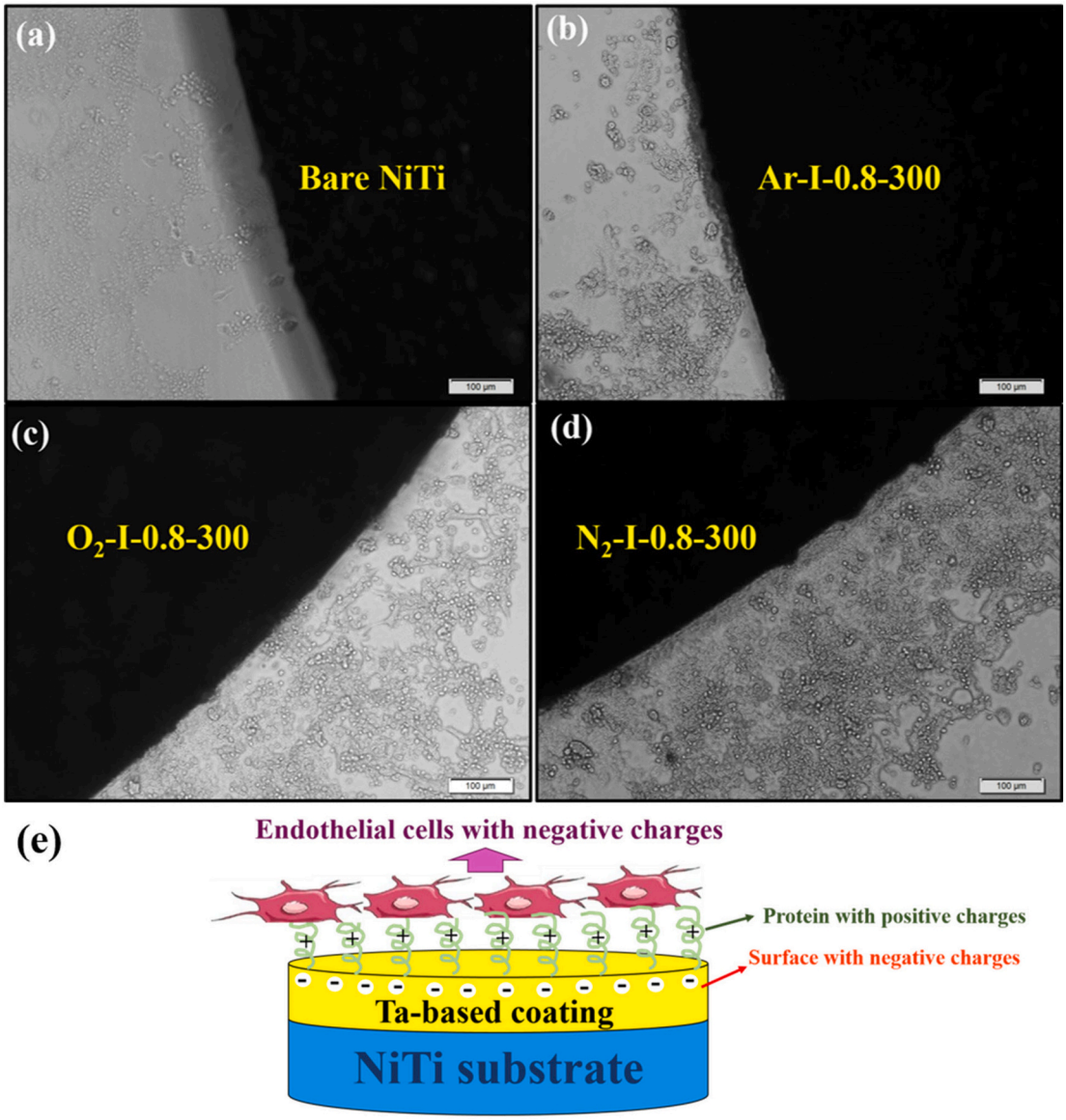


Fig. 12. Optical microscope images of endothelial cells cultured on (a) NiTi substrate, (b) Ar-I-300, (c) O_2-I-300, and (d) N_2-I-300 after 7 days in cell culture along with (e) the schematic of endothelial cells adsorption on coating surfaces.

The optical microscope images of endothelial cells at the interface between the culture medium and coating were shown in Fig. 12 after 7 days of culture. As can be seen in Fig. 12, in complete accordance with MTT assay results, cell proliferation increased from part (a) to (d), respectively. Many empty spots were observed for the NiTi substrate, where no cells were able to grow even after seven days. In contrast, in the N_2-I-300 sample, a favorable environment was provided, so the cells are seen with greater density. The initial cell uptake on a biomaterial in vivo is a well-known phenomenon that occurs through environmental protein adsorption on the implant surface, followed by the attachment of cells to these proteins. The surface charge of a coating is the primary factor that determines the Coulomb interaction between charged components in body fluids [63]. It is shown that the open circuit potential corresponds to the zeta potential difference [62]. In this condition, the N_2-I-300 sample has the most negative open circuit potential (Table 3). As a result, more negative charges were created on the surface of the N_2-I-300 sample, which caused more proteins in the culture medium with a positive charge to accumulate more on the surface of this sample [64]. A schematic of the endothelial cells' adsorption on coated surfaces is shown in part (e) of Fig. 12. As illustrated, proteins serve as a bridge and tend to adsorb more negatively charged endothelial cells towards the surface of the tantalum-based coating, which provides a higher proliferation rate for the cells.

In general, it can be concluded that tantalum thin film deposited in the pure Ar atmosphere has the most promising properties as a biocompatible coating on NiTi alloy employed in stents, and orthodontic wires. Bioactive biomaterials may compromise the function of these applications. Moreover, tantalum oxide and tantalum nitride coatings have bioactivity properties, hence the O_2-I-300 sample can be used for bone fracture plates, and bone staples used temporarily in the body. Additionally, tantalum nitride coatings with higher bioactivity can be used in applications such as artificial bone implants [65].

3.7.2. Apatite formation

Bone and biomaterial integrate faster and more strongly when the apatite layer is present as an interface [66]. The first and second rows in Fig. 13 represent the calcium phosphate formed on the bare NiTi surface and the Ar-I-300 sample after 30 days of immersion in SBF for different magnifications, respectively. Parts (a) and (d) of Fig. 13 show that even after 30 days, only small amounts of calcium phosphate particles were randomly distributed on the surface. The results indicate that both samples are not bioactive, which is expected because of the MTT test outcomes.

3.7.3. Nickel ion release

Based on the release of nickel ions, the samples were assessed from a toxicity perspective. After 30 days of immersion in Ringer's solution at 37 °C, bare NiTi substrate released 10.1 ppb.cm^{-2} nickel ions. Jia et al. [67] reported that nickel ions released from surfaces exposed to the environment for long periods result in the death of surrounding cells. Unlike bare NiTi, all coatings completely prevented the release of nickel ions, resulting in no nickel ions in the solutions and improved biological performance.

4. Conclusions

Amorphous tantalum-containing coatings were deposited using the magnetron sputtering in the atmosphere containing (i) 100 vol% argon, (ii) 16.6 vol% oxygen, 83.4 vol% argon, and (iii) 16.6 vol% nitrogen, 83.4 vol% argon respectively. The results obtained are as follows:

i. Under 100 vol% argon atmosphere, coatings have the most uniform and compact structure, in return, introducing reactive gases (oxygen or nitrogen) to the magnetron chamber produces round-shaped particles on the surface.
ii. XPS results show that; the outermost surface of Ar-I-300 is primarily Ta_2O_5 with a small amount of Ta_2O, whereas Ta_2O_5 dominates the outermost surface of O_2-I-300. Furthermore, most of the outermost layer of the N_2-I-300 sample is made up of TaON, followed by small amounts of Ta_2O.
iii. AFM results demonstrate that the coating deposited under the Ar—N_2 atmosphere exhibited the highest roughness by having R_q = 6.54±0.66 nm.
iv. Among the coated samples, O_2-I-300 has the greatest hydrophilicity by having $\theta_{average} = 75.35^\circ \pm 2.48$, and in return, N_2-I-300 has the most hydrophobic surface by having $\theta_{average} = 115.20^\circ \pm 2.42$.
v. The presence of Ta_2O_5 on the surface of the Ar—O_2 atmosphere leads to the lowest corrosion current density value (1.22×10^{-6}

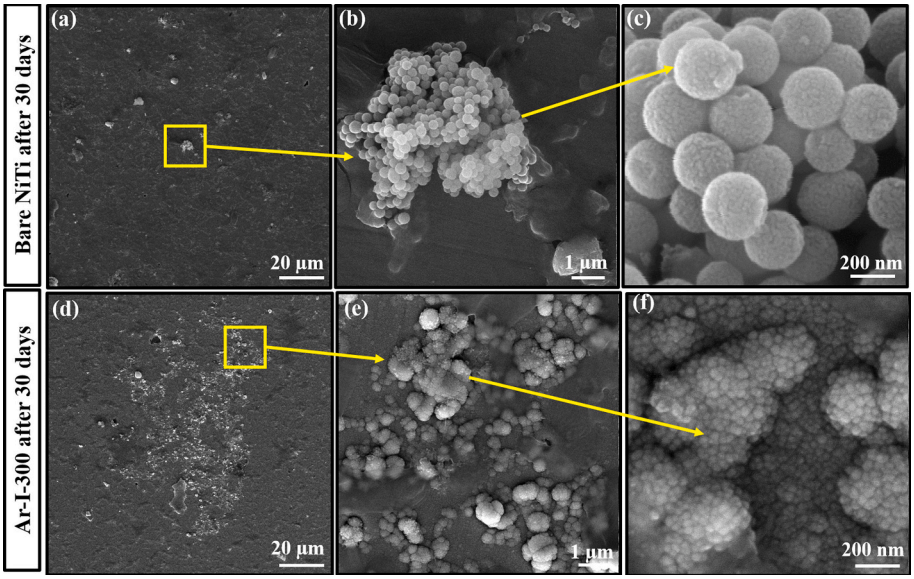


Fig. 13. FESEM images of apatite growth on NiTi surface and Ar-I-300 sample for 30 days of immersion in SBF. Top view FESEM micrograph (a, and d), morphology (b, and e), magnified view (c and, f). The first and second rows in the figure represent the calcium phosphate formed on the bare NiTi surface and the Ar-I-300 sample, respectively.

mA.cm^{-2}), and the highest charge transfer resistance (1.15×10^7 Ω.cm^2).

vi. According to ICP-OES results, all coatings completely prevented Ni ions from leaking out of NiTi substrates after 30 days of immersion in Ringer's solution.

vii. Unlike the toxic behavior of the NiTi substrate, all coated samples exhibited a non-toxic behavior.

viii. Under 100 vol% Ar atmosphere, a pure tantalum coating is deposited, making it biocompatible.

ix. The coating deposited under the Ar—N_2 atmosphere has more negative charges, which increases endothelial proliferation rates.

CRediT authorship contribution statement

Mahdiyeh Soltanalipour: Writing – review & editing, Writing – original draft, Investigation, Data curation, Conceptualization. **Jafar Khalil-Allafi:** Writing – review & editing, Supervision, Project administration, Funding acquisition, Conceptualization. **Amir Motallebzadeh:** Writing – review & editing, Investigation, Data curation, Conceptualization.

Declaration of competing interest

The authors declare that they do not have any competing financial interests or relationships that may have influenced their work.

Data availability

The authors do not have permission to share data.

Acknowledgments

The authors express their sincere thanks and appreciation to “Dr. Hamid Naghshara” (a member of the Physics Department at Tabriz University, Tabriz, Iran) for assisting with the deposition process and using the magnetron sputtering device. We also appreciate “Sahand University of Technology” for financially supporting this research study.

Appendix A. Supplementary data

Supplementary data to this article can be found online at https://doi.org/10.1016/j.surfcoat.2024.130675.

References

[1] M. Soltanalipour, J. Khalil-Allafi, E. Ghareshabani, V. Khalili, Electrochemical behaviour of NiTi alloy coated with TiN using DPF, Surf. Eng. 33 (2017) 1–8, https://doi.org/10.1080/02670844.2017.1283834.

[2] M. Badr, A. Mohammadzadeh, J. Khalil-Allafi, M. Khoshghadam-Pireyousefan, A. Mostafaei, In-situ formation of TiN-TiO2 composite layer on NiTi shape memory alloy via fluidized bed reactor, Ceram. Int. 46 (2020) 21097–21106, https://doi.org/10.1016/j.ceramint.2020.05.184.

[3] W.S. Ko, J.B. Jeon, Atomistic simulations on orientation dependent martensitic transformation during nanoindentation of NiTi shape-memory alloys, Comput. Mater. Sci. 187 (2021) 110127, https://doi.org/10.1016/j.commatsci.2020.110127.

[4] J. Mohd, M. Leary, A. Subic, M.A. Gibson, A review of shape memory alloy research, applications and opportunities, Mater. Des. 56 (2014) 1078–1113. doi: https://doi.org/10.1016/j.matdes.2013.11.084.

[5] S.K. S, I.A. Kumar, L. Marandi, I. Sen, Assessment of small-scale deformation characteristics and stress-strain behavior of NiTi based shape memory alloy using nanoindentation, Acta Mater. 201 (2020) 303–315, https://doi.org/10.1016/j.actamat.2020.09.080.

[6] E. Sgambitterra, C. Maletta, F. Furgiuele, Temperature dependent local phase transformation in shape memory alloys by nanoindentation, Scr. Mater. 101 (2015) 64–67, https://doi.org/10.1016/j.scriptamat.2015.01.020.

[7] D. Stoeckel, A. Pelton, T. Duerig, Self-expanding nitinol stents: material and design considerations, Eur. Radiol. 14 (2004) 292–301, https://doi.org/10.1007/s00330-003-2022-5.

[8] B. Pace, A. Bendavid, M. Ahsan, M. Dargusch, V. Bhatia, J. Byrnes, J. Cairney, Tuning ta coating properties through chemical and plasma etching pre-treatment of NiTi wire substrates, Surf. Coatings Technol. 418 (2021) 127214, https://doi.org/10.1016/j.surfcoat.2021.127214.

[9] Z. Ma, H. Xie, B. Wang, X. Wei, D. Zhao, A novel tantalum coating on porous SiC used for bone filling material, Mater. Lett. 179 (2016) 166–169, https://doi.org/10.1016/j.matlet.2016.05.065.

[10] Y. Zhou, M. Li, Y. Cheng, Y.F. Zheng, T.F. Xi, S.C. Wei, Tantalum coated NiTi alloy by PIIID for biomedical application, Surf. Coatings Technol. 228 (2013) 2–6, https://doi.org/10.1016/j.surfcoat.2012.11.002.

[11] K. McNamara, S. Beloshapkin, K.M. Hossain, M.S. Dhoubhadel, S.A.M. Tofail, Tantalum coating inhibits Ni-migration from titanium out-diffusion in NiTi shape memory biomedical alloy, Appl. Surf. Sci. 535 (2021), https://doi.org/10.1016/j.apsusc.2020.147621.

[12] S. Massey, E. Gallino, P. Cloutier, M. Tatoulian, L. Sanche, D. Mantovani, D. Roy, Low-energy electrons and X-ray irradiation effects on plasma-polymerized allylamine bioactive coatings for stents, Polym. Degrad. Stab. 95 (2010) 153–163, https://doi.org/10.1016/j.polymdegradstab. 2009.11.037.

[13] M.G. Ostapenko, L.L. Meisner, M.A. Zakharova, E.Y. Gudimova, X-ray analysis of the structure-phase states of the tantalum coating on NiTi substrate treated by electron beams, Mater. Today Proc. 2 (2015) S901–S904, https://doi.org/10.1016/j.matpr.2015.07.427.

[14] C. Park, S. Kim, H.E. Kim, T.S. Jang, Mechanically stable tantalum coating on a nano-roughened NiTi stent for enhanced radiopacity and biocompatibility, Surf. Coatings Technol. 305 (2016) 139–145, https://doi.org/10.1016/j.surfcoat.2016.08.014.

[15] K. Tsuchiya, A. Yamamoto, in: M. Niinomi, T. Narushima, M. Nakai (Eds.), Stents: Functions, Characteristics, and Materials, Springer, Berlin, Heidelberg, 2015, pp. 233–250, https://doi.org/10.1007/978-3-662-46842-5_11.

[16] N. Horandghadim, J. Khalil-Allafi, E. Kaçar, M. Urgen, Biomechanical compatibility and electrochemical stability of HA/Ta2O5 nanocomposite coating produced by electrophoretic deposition on superelastic NiTi alloy, J. Alloys Compd. 799 (2019) 193–204, https://doi.org/10.1016/j.jallcom.2019.05.166.

[17] N. Horandghadim, Y. Ghazanfar-Ahari, J. Khalil-Allafi, Multiwalled-carbon nanotubes reinforced hydroxyapatite- tantalum pentoxide nanocomposite coating on nitinol alloy: antibacterial activity and electrochemical properties, Surfaces and Interfaces. 29 (2022) 101773, https://doi.org/10.1016/j.surfin.2022.101773.

[18] S. Asadullah, H. Wu, S. Mei, D. Wang, Y. Pan, D. Wang, J. Zhao, J. Wei, Preparation, characterization, in vitro bioactivity and rBMSCs responses to tantalum pentoxide/polyimide biocomposites for dental and orthopedic implants, Compos. Part B Eng. 177 (2019), https://doi.org/10.1016/j.compositesb.2019.107433.

[19] N. Horandghadim, J. Khalil-Allafi, M. Urgen, Effect of Ta2O5 content on the osseointegration and cytotoxicity behaviors in hydroxyapatite-Ta2O5 coatings applied by EPD on superelastic NiTi alloys, Mater. Sci. Eng. C 102 (2019) 683–695, https://doi.org/10.1016/j.msec.2019.05.005.

[20] N. Horandghadim, J. Khalil-Allafi, M. Urgen, Influence of tantalum pentoxide secondary phase on surface features and mechanical properties of hydroxyapatite coating on NiTi alloy produced by electrophoretic deposition, Surf. Coatings Technol. 386 (2020), https://doi.org/10.1016/j.surfcoat.2020.125458.

[21] J. Khalil-Allafi, H. Daneshvar, M.S. Safavi, V. Khalili, A survey on crystallization kinetic behavior of direct current magnetron sputter deposited NiTi thin films, Phys. B Condens. Matter 615 (2021), https://doi.org/10.1016/j.physb.2021.413086.

[22] M.S. Safavi, M.A. Surmeneva, R.A. Surmenev, J. Khalil-Allafi, RF-magnetron sputter deposited hydroxyapatite-based composite & multilayer coatings: a systematic review from mechanical, corrosion, and biological points of view, Ceram. Int. 47 (2021) 3031–3053, https://doi.org/10.1016/j.ceramint.2020.09.274.

[23] M. Sarraf, A. Dabbagh, B. Abdul Razak, B. Nasiri-Tabrizi, H.R.M. Hosseini, S. Saber-Samandari, N.H. Abu Kasim, L.K. Yean, N.L. Sukiman, Silver oxide nanoparticles-decorated tantala nanotubes for enhanced antibacterial activity and osseointegration of Ti6Al4V, Mater. Des. 154 (2018) 28–40, https://doi.org/10.1016/j.matdes.2018.05.025.

[24] M. Soltanalipour, J. Khalil-Allafi, Superior in vitro corrosion resistance of the novel amorphous ta/TaxOy multilayer coatings on self-expanding nitinol stents, Surf. Coatings Technol. 446 (2022) 128767, https://doi.org/10.1016/j.surfcoat.2022.128767.

[25] M. Soltanalipour, J. Khalil-Allafi, A. Mehrvarz, Study of tantalum-based coatings magnetron sputtered on NiTi alloy in argon and argon/nitrogen atmosphere, Ceram. Int. 50 (2023) 4994–5006, https://doi.org/10.1016/j.ceramint.2023.11.242.

[26] B. Rahmati, A.A.D. Sarhan, W.J. Basirun, W.A.B.W. Abas, Ceramic tantalum oxide thin film coating to enhance the corrosion and wear characteristics of Ti-6Al-4V alloy, J. Alloys Compd. 676 (2016) 369–376, https://doi.org/10.1016/j.jallcom.2016.03.188.

[27] Y.H. Yang, D.J. Chen, F.B. Wu, Microstructure, hardness, and wear resistance of sputtering TaN coating by controlling RF input power, Surf. Coatings Technol. 303 (2016) 32–40, https://doi.org/10.1016/j.surfcoat.2016.03.034.

[28] Z. Ding, Q. Zhou, Y. Wang, Z. Ding, Y. Tang, Q. He, Microstructure and properties of monolayer, bilayer and multilayer Ta2O5-based coatings on biomedical Ti-6Al-4V alloy by magnetron sputtering, Ceram. Int. 47 (2021) 1133–1144, https://doi.org/10.1016/j.ceramint.2020.08.230.

[29] S.S. Firouzabadi, M. Naderi, K. Dehghani, F. Mahboubi, Effect of nitrogen flow ratio on nano-mechanical properties of tantalum nitride thin film, J. Alloys Compd. 719 (2017) 63–70, https://doi.org/10.1016/j.jallcom.2017.05.159.

[30] T. Kokubo, H. Takadama, How useful is SBF in predicting in vivo bone bioactivity ? Biomaterials 27 (2006) 2907–2915, https://doi.org/10.1016/j.biomaterials.2006.01.017.
[31] S. Tsukimoto, M. Moriyama, M. Murakami, Microstructure of amorphous tantalum nitride thin films, Thin Solid Films 460 (2004) 222–226, https://doi.org/10.1016/j.tsf.2004.01.073.
[32] W. Dai, Y. Shi, Effect of bias voltage on microstructure and properties of tantalum nitride coatings deposited by rf magnetron sputtering, Coatings 11 (2021) 0–11. doi:https://doi.org/10.3390/coatings11080911.
[33] T.M. Donovan, K. Heinemann, High-resolution electron microscope observation of voids in amorphous Ge, Phys. Rev. Lett. 27 (1971) 1794–1796, https://doi.org/10.1103/PhysRevLett.27.1794.
[34] N.I. Baklanova, V.V. Lozanov, A.T. Titov, The first evidence of the high oxidation resistance of the novel ternary tantalum-iridium-boron phase, Corros. Sci. 160 (2019) 108178, https://doi.org/10.1016/j.corsci.2019.108178.
[35] X. Chen, R. Bai, M. Huang, Optical properties of amorphous Ta2O5 thin films deposited by RF magnetron sputtering, Opt. Mater. (Amst). 97 (2019), https://doi.org/10.1016/j.optmat.2019.109404.
[36] G. Greczynski, L. Hultman, A step-by-step guide to perform x-ray photoelectron spectroscopy, J. Appl. Phys. 132 (2022), https://doi.org/10.1063/5.0086359.
[37] D. Chittinan, P. Buranasiri, T. Lertvanithphol, P. Eiamchai, V. Patthanasettakul, Observations of the initial stages on reactive gas-timing sputtered TaO thin fi lms by dynamic in situ spectroscopic ellipsometery, Opt. Mater. (Amst). 92 (2019) 223–232, https://doi.org/10.1016/j.optmat.2019.04.040.
[38] B. Díaz, Ś. Jolanta, V. Maurice, M. Pisarek, A. Seyeux, S. Zanna, S. Tervakangas, J. Kolehmainen, P. Marcus, Chromium and tantalum oxide nanocoatings prepared by fi ltered cathodic arc deposition for corrosion protection of carbon steel, Surf. Coat. Technol. 206 (2012) 3903–3910, https://doi.org/10.1016/j.surfcoat.2012.03.048.
[39] I. Perez, V. Sosa, F. Gamboa, J. Trinidad, E. Galindo, J.L. Enríquez, Influence of post - deposition annealing on the chemical states of crystalline tantalum pentoxide films, Appl. Phys. A Mater. Sci. Process. 0 (2018) 0. doi:https://doi.org/10.1007/s00339-018-2198-9.
[40] J. Hirpara, V. Chawla, R. Chandra, Investigation of tantalum oxynitride for hard and anti-corrosive coating application in diluted hydrochloric acid solutions, Mater. Today Commun. J. 23 (2020), https://doi.org/10.1016/j.mtcomm.2020.101113.
[41] A. Jara, B. Fraisse, V. Flaud, N. Fréty, G. Gonzalez, Thin film deposition of ta, TaN and ta/TaN bi-layer on Ti and SS316-LVM substrates by RF sputtering, Surf. Coatings Technol. 309 (2017) 887–896, https://doi.org/10.1016/j.surfcoat.2016.10.067.
[42] M. Sarraf, B.A. Razak, B. Nasiri-Tabrizi, A. Dabbagh, N.H.A. Kasim, W.J. Basirun, E. Bin Sulaiman, Nanomechanical properties, wear resistance and in-vitro characterization of Ta2O5 nanotubes coating on biomedical grade Ti–6Al–4V, J. Mech. Behav. Biomed. Mater. 66 (2017) 159–171, https://doi.org/10.1016/j.jmbbm.2016.11.012.
[43] I. Perez, V. Sosa, F. Gamboa, J. Trinidad, E. Galindo, J.L. Enríquez-carrejo, P. Giovanni, M. González, Effect of ion bombardment on the chemical properties of crystalline tantalum pentoxide fi lms, Vacuum 165 (2019) 274–282, https://doi.org/10.1016/j.vacuum.2019.04.037.
[44] B. Bouchet-Fabre, A. Fadjié-Djomkam, R. Fernandez-Pacheco, M. Delmas, M. Pinault, P. Jegou, C. Reynaud, M. Mayne-L'Hermite, O. Stephan, T. Minéa, Effect of tantalum nitride supporting layer on growth and morphology of carbon nanotubes by thermal chemical vapor deposition, Diamond Relat. Mater. 20 (2011) 999–1004, https://doi.org/10.1016/j.diamond.2011.05.006.
[45] M. Alishahi, F. Mahboubi, S.M. Mousavi Khoie, M. Aparicio, E. Lopez-Elvira, J. Méndez, R. Gago, Structural properties and corrosion resistance of tantalum nitride coatings produced by reactive DC magnetron sputtering, RSC Adv. 6 (2016) 89061–89072, https://doi.org/10.1039/c6ra17869c.
[46] J. Xu, L. Liu, Z.X. De, Promoting bone-like apatite formation on titanium alloys through nanocrystalline tantalum nitride coatings, J. Mater. Chem. B 3 (2015) 4082–4094, https://doi.org/10.1039/C5TB00236B.
[47] A.C. Hee, Y. Zhao, S.S. Jamali, A. Bendavid, P.J. Martin, H. Guo, Characterization of tantalum and tantalum nitride films on Ti6Al4V substrate prepared by filtered cathodic vacuum arc deposition for biomedical applications, Surf. Coatings Technol. 365 (2019) 24–32, https://doi.org/10.1016/j.surfcoat.2018.05.007.
[48] H. Moreira, A. Costa-Barbosa, S.M. Marques, P. Sampaio, S. Carvalho, Evaluation of cell activation promoted by tantalum and tantalum oxide coatings deposited by reactive DC magnetron sputtering, Surf. Coatings Technol. 330 (2017) 260–269, https://doi.org/10.1016/j.surfcoat.2017.10.019.
[49] J. Xu, T. Fu, Y. Lyu, P. Munroe, Z. Xie, In vitro biocompatibility of a nanocrystalline β -ta 2 O 5 coating for orthopaedic implants, Ceram. Int. 44 (2018) 4660–4675, https://doi.org/10.1016/j.ceramint.2017.12.040.
[50] F. Rupp, L. Scheideier, N. Olshanska, M. De Wild, M. Wieland, J. Geis-Gerstorfer, Enhancing surface free energy and hydrophilicity through chemical modification of microstructured titanium implant surfaces, J. Biomed. Mater. Res. - Part A. 76 (2006) 323–334, https://doi.org/10.1002/jbm.a.30518.
[51] R. Yazdi, H.M. Ghasemi, C. Wang, A. Neville, Bio-corrosion behaviour of oxygen diffusion layer on Ti-6Al-4V during tribocorrosion, Corros. Sci. 128 (2017) 23–32, https://doi.org/10.1016/j.corsci.2017.08.031.
[52] S.T. Rajan, M. Das, A. Arockiarajan, In vitro biocompatibility and degradation assessment of tantalum oxide coated mg alloy as biodegradable implants, J. Alloys Compd. 905 (2022) 164272, https://doi.org/10.1016/j.jallcom.2022.164272.
[53] J. Xu, W. Hu, Z.H. Xie, P. Munroe, Reactive-sputter-deposited β-Ta2O5 and TaON nanoceramic coatings on Ti-6Al-4V alloy against wear and corrosion damage, Surf. Coatings Technol. 296 (2016) 171–184, https://doi.org/10.1016/j.surfcoat.2016.04.004.
[54] C.Y. Zheng, F.L. Nie, Y.F. Zheng, Y. Cheng, S.C. Wei, R.Z. Valiev, Enhanced in vitro biocompatibility of ultrafine-grained biomedical NiTi alloy with microporous surface, Appl. Surf. Sci. 257 (2011) 9086–9093, https://doi.org/10.1016/j.apsusc.2011.05.105.
[55] M. Soltanalipour, J. Khalil-Allafi, A. Mehrvarz, A. Kahaie Khosrowshahi, Effect of sputtering rate on morphological alterations, corrosion resistance, and endothelial biocompatibility by deposited tantalum oxide coatings on NiTi using magnetron sputtering technique, J. Mater. Res. Technol. 29 (2024) 3279–3290, https://doi.org/10.1016/j.jmrt.2024.02.098.
[56] S. Yuan, J. Zou, N. Lin, H. Zhang, D. Li, Y. Wu, Understanding the protective role of a gradient titanium oxide ceramic layer on Ti6Al4V against corrosion via analyses of Mott-Schottky curve and electron work function (EWF), Ceram. Int. 48 (2022) 31896–31901, https://doi.org/10.1016/j.ceramint.2022.07.123.
[57] B. Jonathan, Biological performance of tantalum, Clin. Mater. 16 (1994) 167–173, https://doi.org/10.1016/0267-6605(94)90113-9.
[58] H. Koivuluoto, G. Bolelli, L. Lusvarghi, F. Casadei, P. Vuoristo, Corrosion resistance of cold-sprayed ta coatings in very aggressive conditions, Surf. Coatings Technol. 205 (2010) 1103–1107, https://doi.org/10.1016/j.surfcoat.2010.02.052.
[59] J. Liu, M. Lin, M. Hsu, U. Li, Effect of nitriding surface treatment on the corrosion resistance of dental nickel – titanium files in 5. 25% sodium hypochlorite solution, J. Alloy. Compd. J. 475 (2009) 789–793. doi:https://doi.org/10.1016/j.jallcom.2008.08.025.
[60] A.P. Manso, F.F. Marzo, X. Garicano, C. Alegre, A. Lozano, Corrosion behavior of tantalum coatings on AISI 316L stainless steel substrate for bipolar plates of PEM fuel cells, Int. J. Hydrogen Energy 5 (2020), https://doi.org/10.1016/j.ijhydene.2019.12.157.
[61] H. Zhu, X. Ji, H. Guan, L. Zhao, L. Zhao, C. Liu, C. Cai, Tantalum nanoparticles reinforced polyetheretherketone shows enhanced bone formation, Mater. Sci. Eng. C 101 (2019) 232–242, https://doi.org/10.1016/j.msec.2019.03.091.
[62] N. Kobayashi, H. Asakawa, T. Fukuma, Quantitative potential measurements of nanoparticles with different surface charges in liquid by open-loop electric potential microscopy, J. Appl. Phys. 110 (2011), https://doi.org/10.1063/1.3625230.
[63] N. Horandghadim, J. Khalil-alla, Characterization of hydroxyapatite-tantalum pentoxide nanocomposite coating applied by electrophoretic deposition on nitinol superelastic alloy, Ceram. Int. 45 (2019) 10448–10460, https://doi.org/10.1016/j.ceramint.2019.02.105.
[64] G. Xu, X. Shen, Y. Hu, P. Ma, K. Cai, Fabrication of tantalum oxide layers onto titanium substrates for improved corrosion resistance and cytocompatibility, Surf. Coat. Technol. 272 (2015) 58–65, https://doi.org/10.1016/j.surfcoat.2015.04.024.
[65] T. Duerig, A. Pelton, D. Stöckel, An overview of nitinol medical applications, Mater. Sci. Eng. A 273–275 (1999) 149–160, https://doi.org/10.1016/s0921-5093(99)00294-4.
[66] M. Hosseini, J. Khalil-Allafi, M. Etminanfar, M.S. Safavi, N. Bloise, A. Ghalandarzadeh, Tackling the challenges facing the clinical applications of pure PEO hydroxyapatite layers: co-deposition of YSZ nanoparticles, Mater. Chem. Phys. 293 (2023) 126899, https://doi.org/10.1016/j.matchemphys.2022.126899.
[67] W. Jia, M.W. Beatty, R.A. Reinhardt, T.M. Petro, D.M. Cohen, C.R. Maze, E. A. Strom, M. Hoffman, Nickel release from orthodontic arch wires and cellular immune response to various nickel concentrations, J. Biomed. Mater. Res. 48 (1999) 488–495, https://doi.org/10.1002/(SICI)1097-4636(1999)48:4<488::AID-JBM14>3.0.CO;2-D.